JGR Earth Surface

RESEARCH ARTICLE
10.1029/2022JF006850

The Subglacial Lake That Wasn't There: Improved Interpretation From Seismic Data Reveals a Sediment Bedform at Isunnguata Sermia

C. Hofstede[1], F. Wilhelms[1,2], N. Neckel[1], D. Fritzsche[3], S. Beyer[1], A. Hubbard[4,5], R. Pettersson[6], and O. Eisen[1,7]

[1]Helmholtz Centre for Polar and Marine Research, Alfred Wegener Institute, Bremerhaven, Germany, [2]Geoscience Center, University of Göttingen, Göttingen, Germany, [3]Helmholtz Centre for Polar and Marine Research, Periglacial Research Section, Alfred Wegener Institute, Potsdam, Germany, [4]iC3—Centre for Ice, Cryosphere, Carbon and Climate, Institutt for Geosciences, UiT—The Arctic University of Norway, Tromsø, Norway, [5]Geography Research Unit, Oulun yliopisto, Oulu, Finland, [6]Department of Earth Sciences, Uppsala University, Uppsala, Sweden, [7]University of Bremen, Bremen, Germany

Key Points:

- Seismic data show that a subglacial lake implied by high reflectivity in radar data is in fact a lens-shaped sediment bedform
- Seismic reflectivity analysis suggests the lens-shaped bedform is possibly overlain by a thin layer of water-bearing sediments
- The subglacial bedform is stratified and likely deposited through episodically ponding of upstream derived meltwater

Correspondence to:
C. Hofstede,
coen.hofstede@awi.de

Citation:
Hofstede, C., Wilhelms, F., Neckel, N., Fritzsche, D., Beyer, S., Hubbard, A., et al. (2023). The subglacial lake that wasn't there: Improved interpretation from seismic data reveals a sediment bedform at Isunnguata Sermia. *Journal of Geophysical Research: Earth Surface*, *128*, e2022JF006850. https://doi.org/10.1029/2022JF006850

Received 19 JUL 2022
Accepted 24 AUG 2023

Abstract Radio Echo Sounding (RES) surveys conducted in May 2010 and April 2011 revealed a 2 km^2 flat area with increased bed reflectivity at the base of Isunnguata Sermia at the western margin of the Greenland Ice Sheet. This flat reflector was located within a localized subglacial hydraulic potential (hydropotential) minimum, as part of a complex and elongated trough system. By analogy with comparable features in Antarctica, the initial interpretation of such a feature was a potential subglacial lake. In September 2013 a co-located seismic survey revealed a 1,750 m by 540 and 37 m thick stratified lens-shaped bedform at the base of a subglacial trough system. Amplitude Versus Angle (AVA) analysis yields a derived reflection coefficient $R = 0.09 \pm 0.14$ indicative of consolidated sediments possibly overlain by dilatant till. The bed and flank on the northern side of the trough consist of unconsolidated, possibly water-bearing sediments with $R = -0.10 \pm 0.08$, whereas on the southern side it consists of more consolidated material. We interpret the trough as a key component of the wider subglacial drainage network, for which the sediments on its northern side act as a localized water-storage reservoir. Given the observation of seasonally forming and rapidly draining supraglacial meltwater lakes in this area, we interpret the lens-shaped bedform as deposited by episodically ponding meltwater within the subglacial trough system. Our results highlight the importance of transient subglacial hydrological and sedimentological processes such as drainage events for the interaction of ice sheets and their substrates, to understand ice dynamics in a warming climate.

Plain Language Summary A ground based radar survey in West Greenland showed an unusually flat, highly reflective zone in an otherwise rough bed suggesting a possible subglacial lake beneath the ice. The highly reflective zone was part of a drainage system transporting meltwater under the ice sheet. We performed a detailed seismic survey across the area which, unlike radar signals, has the advantage of penetrating through the overlying ice into any rock, sediments and water below it. Analysis of our reflection data reveal that the flat area was in fact an elongated lens-shaped bedform consisting of layered (stratified) sediments. However at a larger angle of incidence, analysis showed the bedform is possibly overlain by a thin layer of water-bearing sediments likely saturated by ponding water. Our interpretation is that episodically draining meltwater from upstream is locally accumulating beneath the ice sheet at this locality, thereby depositing the lens-shaped bedform over many melt seasons.

1. Introduction

To understand the dynamic behavior of ice sheets quantifying the basal drag is essential. Quantifying the basal drag of ice sheets is difficult because it varies over time and place. This variation is largely caused by variation in subglacial water either present in porous subglacial sediments, linked cavities, channelized system or subglacial lakes. Pressurized water reduces basal drag by carrying the weight of the overlying ice. For the Greenland Ice Sheet (GrIS) surface melt, run-off, englacial drainage to the bed, bed conditions (material and topography), ice thickness and surface topography determine the subglacial drainage network (SDN) which influences the basal motion and mass loss of the ice sheet. This SDN was originally thought to vary over time and place between two end members: an inefficient drainage system and an efficient channelized drainage system, as observed at alpine

glaciers (Hubbard & Nienow, 1997) whereby the basal friction, and as a consequence the ice flow, depend on evolution of the SDN.

Using the same terminology as proposed by Davison et al. (2019) we distinguish an early, late and post melting season that vary over time and place on the ice sheet. We refer to areas within 50 km from the ice margin and from 50 km to the equilibrium line as lower and upper ablation area and further inland as lower accumulation area.

The ablation zone of the land terminating Kangerlussuaq sector experiences an annually returning ice motion evolution thought to be triggered by drainage of the annual melt. On a seasonal time scale the early melt season is characterized by a speed-up of ice velocity (Bartholomew et al., 2010; Joughin et al., 2008), also known as the "spring event" (van de Wal et al., 2015). The hypothesis is that the SDN is not efficient enough to discharge the melt water peaks. Excess water at the bed is pressurized, reducing the basal friction at the bed leading to the speed-up. As the melt season progresses into late summer and early autumn, the ice velocity slows to a minimum (Sole et al., 2013; van de Wal et al., 2015). By now a steady supply of meltwater reaches the bed, the SDN becomes more efficient, the water pressure at the bed reduces and the basal friction at the bed increased. Over winter the ice velocity slowly increases to the pre-melt season velocity. For the more interior parts of the ice sheet the melt season starts later and is shorter thus shortening the time to build-up an efficient SDN. The drainage network is also less efficient due to higher ice overburden pressure and a smaller hydraulic gradient due to a lower ice surface slope (Doyle et al., 2014; Tedstone et al., 2015).

However, on decadal time scale, despite increased surface melt, the area experienced a slow-down since 2007 in comparison to the 1985–1994 period (Tedstone et al., 2015). The SDN is assumed to have increased its efficiency due to increased melt inland over longer time scales and this process is referred to as self-regulating ice flow.

Self-regulating ice flow ignores the complex role subglacial sediments may have as the strength of these subglacial sediments depends on its subglacial water storage and its sensitivity to the time-varying hydraulic gradient. Subglacial sediments may exert a dominant control on the time varying ice flow (Bougamont et al., 2014). According to Ryser et al. (2014) ice flow in the ablation zone is controlled by activation of basal patches of varying slipperiness. A 10 m thick subglacial sediment patch with varying slipperiness controlled the ice motion of an area five times the ice thickness. To explain the long timespan of the ice velocity slow down, Hoffman et al. (2016) introduced hydraulically weakly connected regions, explaining the slow ice sheet response to increased melt periods and the observed low hydraulic connectivity of boreholes in close proximity to each other. As Kulessa et al. (2017) summarized, self-regulation of mean annual ice flow or ice flow controlled by soft subglacial sediments result in different long term ice flow evolution in a warming climate: self-regulation results in a slowdown whereas ice flow controlled by soft subglacial sediments results in acceleration. It is thus important that we know the strength and its water saturation dependency of the subglacial material to predict ice flow.

Subglacial lakes can be part of the SDN. Bowling et al. (2019) presented an inventory of 54 possible and four existing subglacial lakes at Greenland, dividing them in stable, hydrologically active, hereafter referred to as active subglacial, and seasonally active, hereafter referred to as seasonal subglacial lakes. The active subglacial lakes and seasonal subglacial lakes are part of the SDN. Active subglacial lakes are thought to form near the Equilibrium Line Altitude (ELA) and are recharged by surface meltwater finding its way to the base. Seasonal subglacial lakes form over winter below the ELA, and drain during the melt season (Livingstone et al., 2019; S. J. Palmer et al., 2013; S. Palmer et al., 2015). Livingstone et al. (2022) updated the inventory of Greenland's subglacial lakes to 64, identifying five filling and draining patterns (defining a ratio of filling and draining) in the active subglacial lakes. It is the temporary storage and release of subglacial water to the SDN causing variation of basal friction over time and place of the subglacial area affected by storage and drainage that makes active subglacial lakes important. They can be seen as time varying areas of basal drag of and ice sheet.

A problem ice sheet modelers have is the lack of observations of the subglacial conditions. They are mostly restricted to point observations (boreholes), the ice–bed contact (radar) or with limited lateral extend (passive and active seismic observations). One such study (Harper et al., 2017) revealed a surprising lack of soft subglacial sediments, but an abrupt ice–hard bed transition where Bougamont et al. (2014) modeled a soft sediment bed. As a result numerical and conceptual models lack much needed confirmation of their theoretical frameworks.

In this paper we present observations of the subglacial environment in the upper ablation zone of Isunnguata Sermia in the Kangerlussuaq sector of the GrIS. In the study area radio-echo sounding (RES) surveys reveal a hydraulically flat specular bed and a basal reflectivity that would be consistent with a possible subglacial lake

based on the criteria of Bowling et al. (2019). However, interpretation of coincident active seismic surveys reveal that this feature is likely a sedimentary feature. Thus, our results urge caution when interpreting RES for the presence of subglacial lakes.

2. Field Site and Methods

2.1. Field Site

The field site (N 67.0334, W 48.6241) lies in the upper ablation area, 70 km upstream of the terminus of Isunnguata Sermia, a land terminating, well-studied glacier in the Kangerlussuaq sector in West Greenland (Figure 1). Here the ice sheet reaches an elevation of 1,380 m, is some 1,250 m thick and lies 20 km west of the Equilibrium Line at approximately 1,550 m (van de Wal et al., 2012). The area is characterized by active supraglacial lake drainage after the Fitzpatrick et al. (2014) study who observed the area from 2002 to 2012. The ice flow is variable but on average around 90 m/a in westerly direction and is largely controlled by subglacial meltwater and the efficiency of the drainage network (van de Wal et al., 2015). The field site is characterized by closed former crevasses and/or water-filled (frozen) partial depth hydrofractures (Chandler & Hubbard, 2023) mostly orientated parallel to the ice flow direction as indicated by the seismic data (Figures 3c and 4c). In 2010 the spring event took place at 25–28 May followed by a cluster of supraglacial lake drainage at 6–10 June leading to a sudden loss of basal traction and ice flow speed-up (Christoffersen et al., 2018; Fitzpatrick et al., 2014). In July 2010 nearby supraglacial lake F, approximately 5 km SW of our survey site, drained rapidly through a glacial fracture driving localized uplift of almost 1 m due to hydraulic jacking (Doyle et al., 2013; Kulessa et al., 2017).

2.2. Radio-Echo Soundings

On 20 May 2010 and 28 April 2011 two RES surveys at this area of Isunnguata Sermia were performed (Figure 1). The RES surveys were made with a ground-based 2.5 MHz impulse RES-system with loaded dipole antennas. The RES surveys were part of a larger RES survey described by Lindbäck et al. (2014) where a technical description of the radar and the processing of the RES data can be found. However, the profiles collected in April 2011 that are presented in this paper are not included in the Lindbäck et al. (2014) data set. These data were further analyzed to determine the subglacial hydropotential field and hydrological network, which revealed a transient SDN characterized by numerous subglacial lakes and active subglacial drainage piracy between Isunnguata Sermia and its adjacent outlet glaciers (Lindbäck et al., 2015).

In this study, we investigate the properties of the ice-bed contact using the relative basal reflectivity (Figure 1b). The relative basal reflectivity was estimated from the bed return wavelet after correcting for geometrical spreading and the attenuation from dielectric losses with in the ice column. The two-way depth-average attenuation rate through the ice was estimated to 23.3 ± 1.5 dB/km using the method of Jacobel et al. (2009). The attenuation rate can also be estimated from ice chemistry and temperature (MacGregor et al., 2007). Using their method, we estimated the attenuation rate to 24.2 dB/km based on vertical temperature profile in an 800 m bore hole collected 35 km northwest of our study area (Harrington et al., 2015) and the chemistry of pure ice.

2.3. Seismic Data Acquisition and Processing

In September 2013 we performed a targeted seismic reflection survey (Figure 1) consisting of two, ∼5 km perpendicular profiles. We recorded the seismic data using a 212 m (190 m active spread), 96 seismic channels, snow streamer behind a Nansen sled, towed by a snow mobile. Each channel consisted of a gimbaled 30 Hz vertical component sensor. For recording we used four seismographs (Geometrics, GEODE) each recording 24 channels, and a recording laptop which were strapped onto the Nansen sled. Using a sample interval of 0.25 ms and a record length 3 s, we recorded data to approximately 3 km below the ice surface. This set-up enabled us to reposition the channels by simply pulling the streamer over the surface to a new recording position. As a source we used 500 g dynamite cartridges placed in 2 m deep boreholes. Shots were fired in front of the streamer at a fixed offset of 12 m. With a shot spacing of either 50 or 100 m we collected single- to 2-fold data.

We processed the data using the following standard processing techniques: static corrections, top mute to remove direct waves, trace editing, spiking deconvolution, frequency-wavenumber filtering (FK: −1.05–1.05 Hz/m), band-pass filtering (Butterworth filter: 30–550 Hz), Normal-Move-Out (NMO) correction with 65% stretch mute,

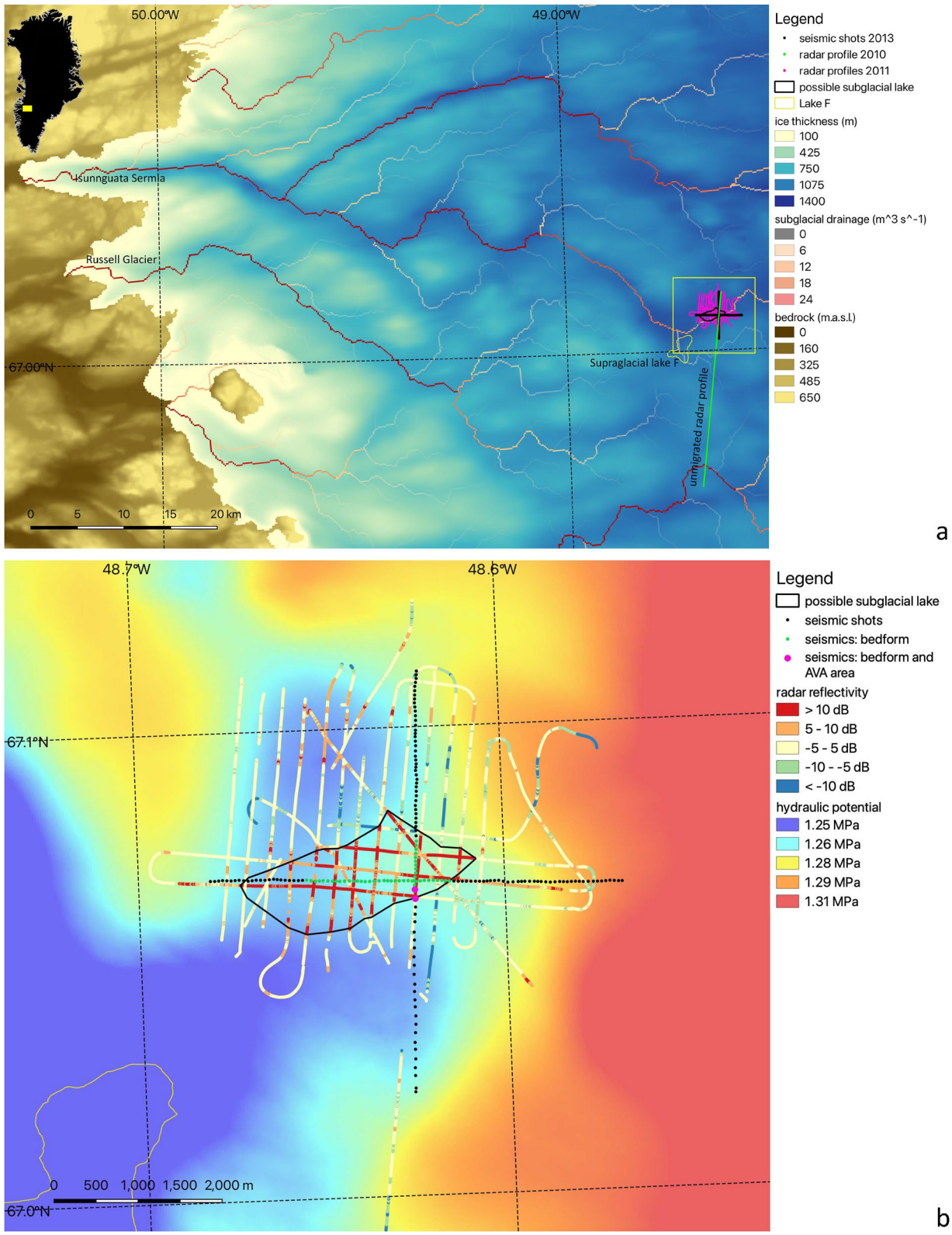

Figure 1.

Table 1
V_P Determined From a Velocity Analysis of Four Horizons From the 8-Fold Covered AVA Area

Time (ms)	Stacking velocity (m/s)	Interval velocity (m/s)	Accuracy pick (m/s)	Medium
475	3,845	3,845	–	Ice
630	3,845	3,845	–	Ice
654	3,845	3,845	±50	Ice
667	3,820	2,225	±400	Sediments

stacking and time migration (Kirchhoff-migration, maximum dip 40°). We performed an interactive (NMO) velocity analysis using four horizons (at 475, 630, 654, and 667 ms, Table 1) of the 8-fold AVA data set which we assumed to be representative for the whole area.

2.4. The Seismic Reflection Coefficient

Angle dependent reflectivity at an interface of two half-spaces depends on contrasts in P-wave velocity V_P, S-wave velocity V_S, density ρ and angle of incidence θ (Aki & Richards, 2002). To identify the subglacial material we used the seismic reflectivity of the bed of both the single shot records for a normal incidence analysis and a long offset Common Midpoint gather consisting of eight (nine shots includes one misfire) shots for a θ-dependent analysis.

With our in Section 2.3 mentioned snow streamer Nansen sled geometry having a offset range of 22–212 m and a target depth between 1,075 and 1,270 m, we assume reflections of single shot records are normal incidence ($0.5° \leq \theta \leq 5.6°$). Under these conditions the seismic reflection coefficient R is solely determined by the contrast of the acoustic impedance ($Z = \rho V_p$) of the media interface:

$$R = \frac{Z_2 - Z_1}{Z_2 + Z_1} = \frac{\rho_2 V_{p_2} - \rho_1 V_{p_1}}{\rho_2 V_{p_2} + \rho_1 V_{p_1}}, \quad (1)$$

where subscripts 1 and 2 refer to upper and lower media. At the ice–bed contact the acoustic impedance of the upper medium (medium 1, $Z_1 = (3.20 \pm 0.05) \times 10^6$ kg m^{-2}s^{-1}) is known as it is ice so if we determine R the acoustic impedance of the subglacial material (medium 2) can be determined. To do this we determined the θ-dependent reflection coefficient $R(\theta)$ from the band pass filtered (BP, 30–550 Hz) shot records:

$$R(\theta) = \frac{A_1(\theta)}{A_0} r(\theta) e^{\alpha r(\theta)}, \quad (2)$$

with $A_1(\theta)$ being the amplitude of the primary reflection of the considered interface and A_0 being the source amplitude, $r(\theta)$ the length of the ray path of the primary wave, whereby we consider the ice as a single layer medium, and α the seismic attenuation coefficient. We determined the polarity of the amplitude from polarity of the direct wave (Appendix A). The seismic attenuation (α) of the entire ice layer ($\alpha = 0.2$ km^{-1}) was derived by adopting the same P-wave seismic quality factor Q as Booth et al. (2012) derived as their survey area was 5 km away from ours.

Determination of A_0 can be done by several methods: either using the exponential decay of the direct wave (direct wave method) or comparing the primary and first multiple reflection (Holland & Anandakrishnan, 2009) (multiple bounce method). Horgan et al. (2021) investigated several methods concluding the multiple bounce method is preferable. We compared two methods, one quantifying the exponential decay of the direct wave and extrapolating this to the source location with the multiple bounce method. Both methods assume continuity of the upper medium (ice) but the ray paths are different. For the single shot records the ray path of the multiple closely resembles that of the primary reflection and so the multiple bounce method has preference but could only be applied at four locations whereas the direct wave method can be applied at each shot location. However, the survey area is characterized by closed crevasses orientated parallel to the ice flow mainly giving discontinuities in the ice surface of the across-flow profile and thus affecting the direct wave. For the direct wave method we restricted ourselves to 10 shots of the along-flow profile, picking the peak amplitude value of the direct wave or the considered reflection. Comparing both methods gave an average value of $A_0 = 5{,}200$ with a standard deviation, $\sigma = 1{,}355$ for the multiple bounce method and $A_0 = 5{,}800$ with $\sigma = 960$ for the direct wave method. Both methods give comparable results but as the direct wave method covers a larger area of the survey it gives a more representative average value so in our calculations we used $A_0 = 5{,}800$ with $\sigma = 960$.

Figure 1. The seismic survey of 2013 and radar surveys of 2010 (Figure 2) and 2011 at Isunnguata Sermia in West Greenland (see black inset). (a) The surveys (radar 2010 green dots, radar 2011 pink dots, seismics 2013 black dots) are plotted over the bedrock (Lindbäck et al., 2014) and semitransparent ice surface data. Plotted over the subglacial trough system is the meltwater flux determined by a subglacial water routing model. The flat area with increased reflectivity is marked by the black polygon and supraglacial Lake F (Doyle et al., 2013) by the yellow polygon. (b) A zoom of the survey area plotted over the hydropotential. The radar reflectivity is now represented by the blue to red colored dots whereby red resembles increased reflectivity (>10 dB). The seismic shots are marked by the black, green and pink dots. The crossing of the seismic along- and across-flow profiles lies over the target area. Green and pink dots represent shots that show the bedform. The AVA area is marked by the larger pink dots.

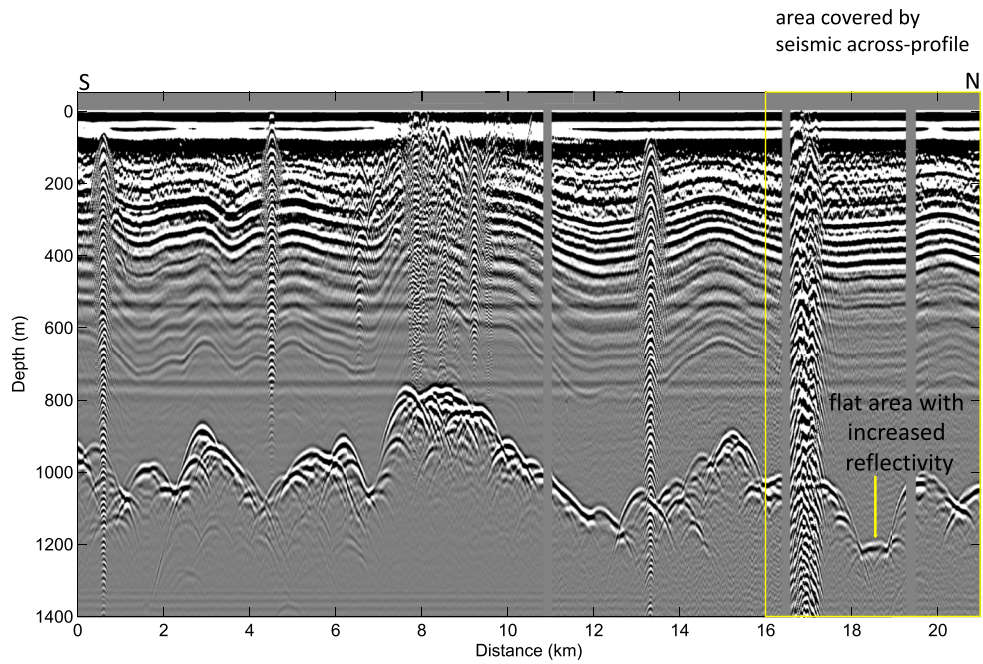

Figure 2. The unmigrated radio-echo sounding profile (Figure 1a) collected in May 2010. The profile is shown unmigrated because surface reflections (seen as vertical stacked reflections along the profile) are obscuring the data in the migrated section making the overall profile less clear. The section that is approximately covered by the seismic across-flow profile is marked in the yellow rectangle (between km 16 and 21).

At the crossing of the two seismic profiles in across-flow direction we investigated $R(\theta)$ over the range $0° \leq \theta \leq 40°$ of the ice–bed contact. This analysis is referred to as Amplitude versus Angle (AVA)—analysis and the "Knott-Zoeppriz" (KZ)-equations (Aki & Richards, 2002) describe $R(\theta)$ at a media interface. We collected a long-offset CMP-gather consisting of eight shots in across-flow direction (Figure 6). Shots and receivers were moved in opposite but equal distances from the considered midpoint (crossing of the profiles), increasing the near trace offset in steps of 100 m so the long-offset gather covers a continuous offset range from 0 to 1,800 m ($0° \leq \theta \leq 40°$) and is assumed to cover the same reflection area (the pink dots of Figure 1b). The assumption here is that the physical properties of the interface (ice–bed contact) do not change within the reflection area or during the survey time and that only the two considered media at the interface influence $R(\theta)$.

We calculated the uncertainty of $R(\theta)$ using standard deviations of three variables: A_0, A_1, and $r(\theta)$. The uncertainty in A_1 was determined by the average noise level of a preceding 10 ms window and the uncertainty of $r(\theta)$ we derived from the error in the ice velocity (Table 1).

2.5. Modeled Subglacial Water Routing

We modeled the subglacial water routing system of the survey area by the hydropotential Φ (Shreve, 1972):

$$\Phi = \rho_w g h_b + \rho_i g H, \tag{3}$$

where ρ_w is the density of water, g acceleration due to gravity, h_b bed elevation (Morlighem et al., 2017), ρ_i density of ice and H the ice thickness. Using the assumption that the basal water pressure and ice overburden pressure are in equilibrium, we used a flux routing scheme to compute hydrologic pathways (Humbert et al., 2018; Lindbäck et al., 2015). In combination with the hydropotential Φ this allowed us to not only to identify potential subglacial lake locations at local sinks in the hydropotential (Figure 1b), but also to indicate sinks that are more likely to be filled with water because they are connected to the hydrologic network. The water input needed for this routing scheme is comprised of subglacially produced water (basal melt plus melt generated from internal shear) and surface water that reaches the base through intraglacial pathways (e.g., crevasses and moulins). We used basal water computed from a high-resolution ice dynamics model (PISM; Aschwanden et al., 2016) and took surface melt and runoff from a regional atmospheric climate model (RACMO2.3p2; Noël et al., 2019). We assumed that

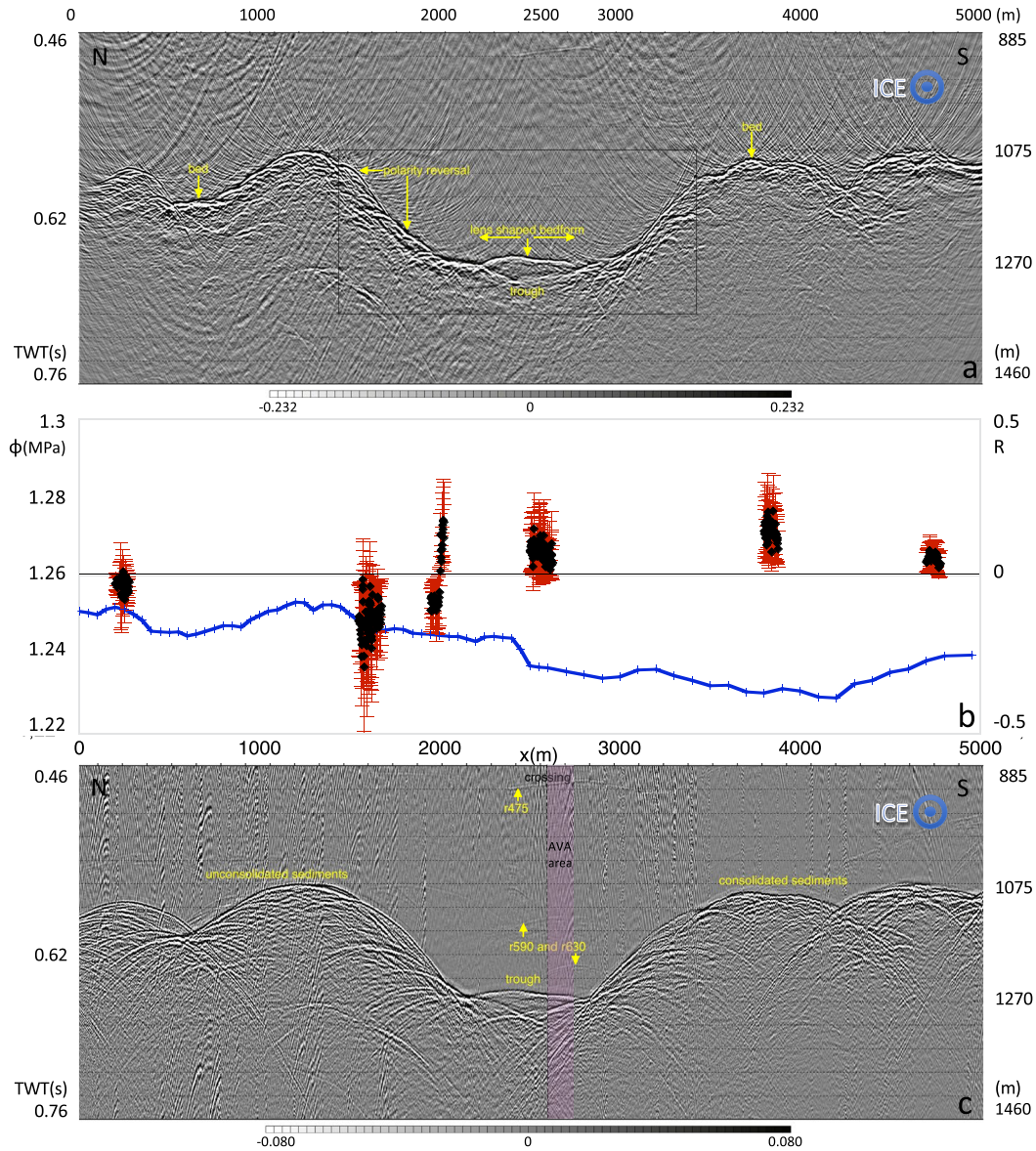

Figure 3. The across-flow profile: (a) The (Kirchhoff) migrated stack which best represents the subglacial geometry but reduces amplitude information. Inset box shows the location of Figure 5a. The lens-shaped bedform is clearly visible as a separate feature at the bed of the trough. (b) The reflection coefficient R at normal incidence (black dots with red arrow bars, right y-axis) determined from eight single shots and hydropotential Φ (blue line, left y-axis) along the seismic profile. The horizontal black line marks $R = 0$. (c) The BP-filtered stack where we indicate three englacial reflections, r475, r590, and r630, named after their TWT. The pink transparent rectangle represents the AVA area of the bed where $R(\theta)$ is determined. The vertical black dashed line marks the crossing of both profiles.

85% of the surface water reaches ice base and, ignoring any intraglacial transport, add it to the basal water. This approach may lead to some overestimation of water flux in our study area (Koziol et al., 2017).

3. Results

3.1. Radar Bed Reflectivity and Subglacial Water Routing

The RES surveys of May 2010 reveal a flat area (Figure 2) with increased reflectivity that is part of a larger subglacial trough system described by Lindbäck et al. (2014). Additional RES profiles, collected in April 2011 (Figure 1), determined the spatial extent of the flat area and were processed following the method of Lindbäck

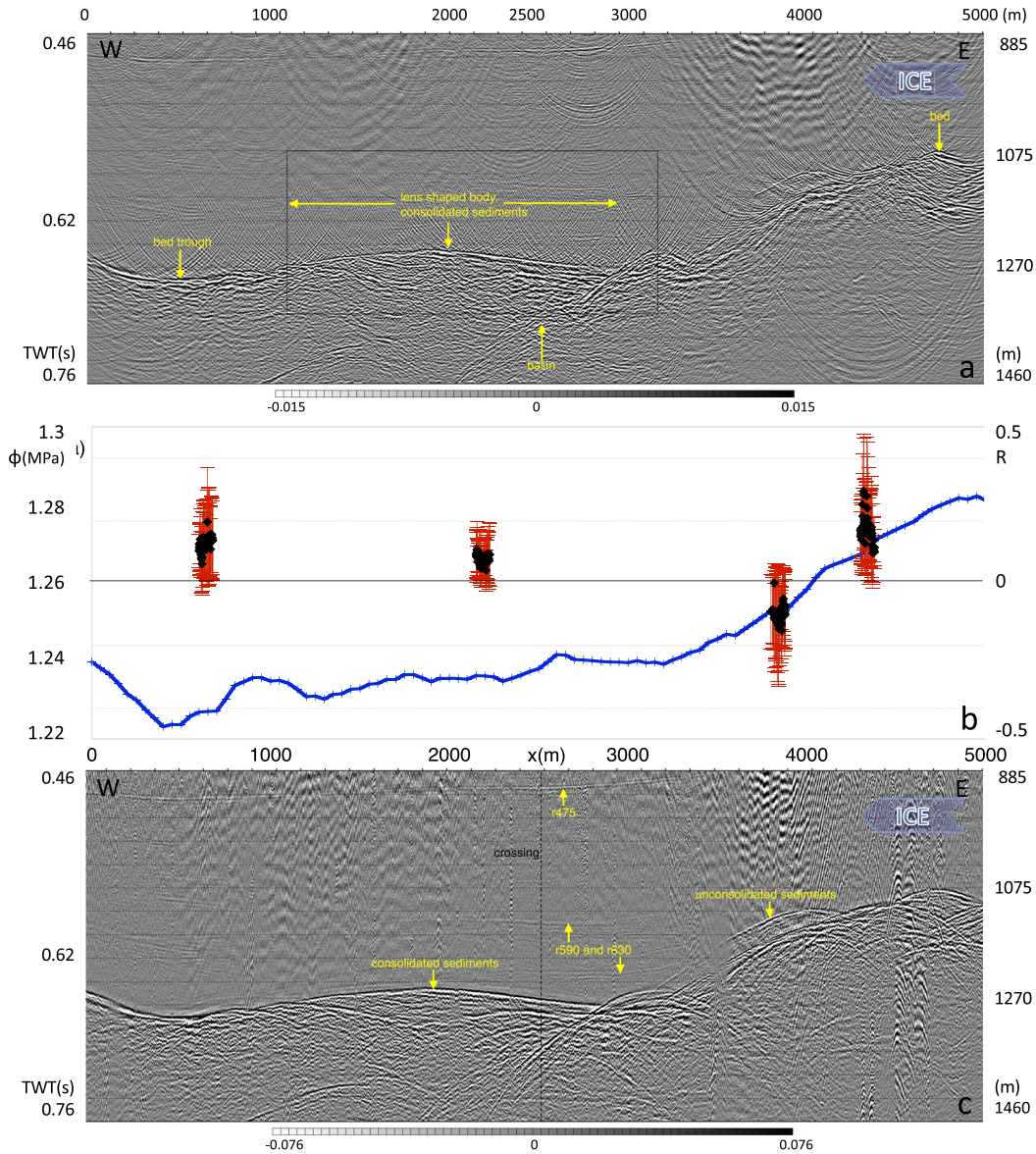

Figure 4. The along-flow profile: (a) The migrated stack showing the elongated lens-shaped bedform at the bed of the trough system. Inset box shows the location of Figure 5b. Below the lens-shaped bedform at the upstream site we see a ~800 m long and ~60 m thick sediment basin. (b) The reflection coefficient R at normal incidence (black dots with red arrow bars, right y-axis) determined from single shots at four locations and Φ (blue line, left y-axis) along the seismic profile. The horizontal black line marks $R = 0$. (c) The BP-filtered stack where we indicated three englacial reflections, r475, r590, and r630, all sub-parallel to the bed. The vertical black dashed line marks the crossing of both seismic profiles.

et al. (2014). The flat area had a basal reflectivity (>10 dB) exceeding 1σ, 2σ, or 3σ above the mean reflectivity within a 10 km radius surrounding region, consistent with previous interpretations of a possible subglacial lake (Bowling et al., 2019; Carter et al., 2007).

The modeled subglacial water routing (Figure 1a) generally follows the subglacial trough system identified by Lindbäck et al. (2014) and the transient hydropotential routing analysis of Lindbäck et al. (2015), using variable subglacial water pressures, varying from 80% to 110% of overburden pressure. Our results are in broad agreement with the Lindbäck et al. (2015) reconstruction of the SDN assuming subglacial water pressure equals overburden pressure, but occasionally fall short in correctly identifying the emerging proglacial portals at the ice margin. The area with increased reflectivity is part of this trough system and lies almost at a local minimum of Φ (Figure 1b).

Both radar survey and modeled subglacial water routing characterize the area as a possible subglacial lake. To verify this we performed the active seismic survey.

3.2. Active Seismic Data

Figures 3 and 4 present the across- and along-flow profiles in the following way: The time migrated (Kirchhoff) stack (Figures 3a and 4a), best representing the subglacial topography, a combined graph (Figures 3b and 4b), showing the reflection coefficient $R(\theta)$ calculated (Equation 2) at normal incidence (left y-axis) and Φ (right y-axis) calculated (Equation 3) using the bed and surface topography derived from the seismic profiles and a BP-filtered stack (Figures 3c and 4c). Thereby we aimed to preserve the amplitude information, englacial reflections and reflected direct waves (causing diamond shaped patterns) as well as possible. The direct waves were later removed with the FK-filter. When discussing features, we use the distance along the profile and refer to depth as depth below the ice surface.

The bed of the 5,000 m long across-flow profile (Figure 3a) lies at 1,075 m depth, and at 1,270 m in the center at 2,500 m where there is a 2 (top) to 1 km (base) wide, 195 m deep, trough. As the migration aperture is ∼900 m, out of plane reflections did not affect the migration. The bed is characterized by short wavelength (1 km) topography (amplitude ∼40 m). The bed on either side of the trough indicates a thin layer of 10–20 m stratified material consisting of discontinuous and chaotic reflections although at end of southern side the migration has distorted the structure and is dominated by "smiles" that are mainly caused by the abrupt amplitude variation along the bed. There is no deeper structure visible. The bed of the trough lacks stratification. At its center, at 2,500 m, there is an ∼540 m wide, ∼20 m (Table 1) high lens-shaped bedform, clearly separated from the bed, with little stratification (Figure 5a).

Figure 3c shows the BP-filtered (30–550 Hz) stack showing the same features: the ice–bed contact at 1,075 m depth reaches a depth of 1,270 m at the trough. As the data is not migrated, bumps appear wider and less steep, the trough appears narrower and the lens-shaped bedform now seems to cover the entire base of the trough. The amplitude information is better preserved simply because the data have been processed less. The ice–bed contact on the northern side of the trough and especially the northern flank of the trough clearly show a reversed (white and negative) polarity compared to the trough itself and the bed south of it (black and positive, Appendix A). The polarities of the top (ice–bedform contact) and bottom (bedform–bed contact) of the bedform are both positive.

The ice above the bed on the northern side and above the trough are characterized by diamond shaped patterns consisting of two sets of linear dipping, source induced, noise (dipping in and opposite to the shooting-direction) caused by reflections of the direct wave reflecting against (probably) closed crevasses in front of and behind the snow streamer (Figure 3c and Figure A1). These patterns are clearly present at the northern side of the trough and at the trough itself (0–3,000 m). Coinciding with the diamond shaped patterns we see hyperbolas in the ice, caused by point scatterers, possibly crevasses. At the southern flank of the trough the pattern is dominated by, in the shooting direction, linearly dipping, source induced noise coming from behind the snow streamer (3,000–3,600 m). Otherwise the ice south of the trough shows much less of this source induced noise. In the ice we distinguish three reflections named after their two-way travel time (TWT): r475, r590, and r630 at respectively 913 m, 1,134 m, and 1,211 m depth at the reflection area of the AVA data set marked by the pink rectangle. Reflection r475 roughly follows the shape of the ice–bed reflection and lies some 250 m above the bed outside the trough. Reflections r590 and r630 are concave-shaped like the ice–bed reflection but have a weaker reflection.

We determined R at normal incidence (Figure 3b) at eight shots, showing up as six locations. The across-flow profile can be subdivided into the area north of the trough with $R < 0$ and the trough with its area south of it having $R > 0$. The reversal of the polarity of R abruptly takes place at the transition of the northern flank (at ∼2,000 m) with $R < 0$ to the base of the trough and the bed south of it with $R > 0$. At the bed north of the trough, at 230 m, $R \approx -0.05 \pm 0.07$ and at 1,600 m $R \approx -0.15 \pm 0.09$. At the northern flank at 2,000 m, $R \approx -0.09 \pm 0.09$ increasing to $R \approx 0.09 \pm 0.11$ at 2,100 m. At the lens-shaped bedform at 2,500 m, $R \approx 0.09 \pm 0.14$. At the bed south of the trough at 3,800 m $R \approx 0.15 \pm 0.14$ and at 4,750 $R \approx 0.05 \pm 0.05$. We calculated Φ (Equation 3) from the derived ice thickness and the bed topography and plotted Φ in the same graph on the left y-axis. From north to south at the across-flow profile Φ decreases by ∼20 kPa with its maximum at ∼1,400 m and its minimum at ∼4,200 m. The lowest values of Φ are between 2,500 and 4,200 m.

We discuss the along-flow profile (Figure 4a) in ice flow direction from east to west (opposite to the shooting direction). The bed at the eastern side at 5,000 m lies ∼1,100 m depth, descends from 4,000 to 3,000 m to

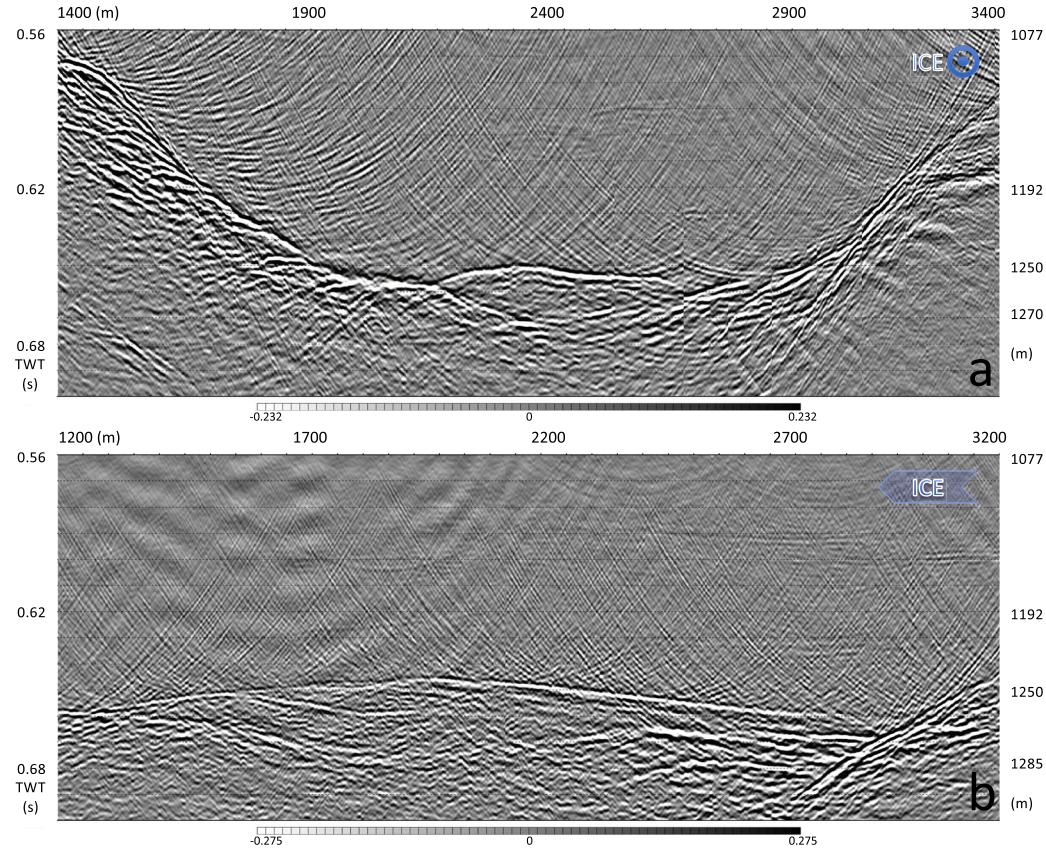

Figure 5. A zoom of the lens-shaped bedform, both across- and along-flow: (a) Zoom of the lens-shaped bedform of the migrated across-flow profile (Figure 3a). The lens-shaped bedform clearly lies on top of the bed in the trough system and is 540 m wide. (b) Zoom of the lens-shaped bedform of the migrated along-flow profile (Figure 4a). The lens-shaped bedform is 1,750 m long.

1,270 m depth as it enters the subglacial trough system. At the eastern side at 5,000 m the bed shows a ~100 m stratified sequence at a local depression consisting of chaotic discontinuous reflections but also here migration has distorted the structure making interpretation difficult. At 4,200 m two dipping reflectors show the bed starts to descend into the trough from which the upper dipping reflector has a reversed polarity. The ice–bed transition here and throughout the descent shows no sign of stratification. At 3,500 m the bed of the trough lies at 1,270 m depth. The 1,750 m long lens-shaped bedform lies between 3,000 and 1,250 m (Figure 5b). The bed here is smooth, gently rising to 1,230 m depth (stoss side) at 1,900 m where the lens-shaped bedform reaches a thickness of ~37 m (V_P = 2,225 m/s, Table 1). The little stratification there is (mainly at the top and bottom of the lens-shaped bedform) is parallel to the ice–bed contact. At the lee side the bedform gently lowers to 1,270 m depth at 1,150 m where the lens-shaped bedform terminates and stratification is truncated. At 600 m the bed reaches a maximum depth of 1,290 m depth. Below the onset lens-shaped bedform at 2,500 m there is a 800 m long, ~55 m thick, basin having a stratified sequence consisting of a dense sequence of chaotic reflections showing little amplitude loss with depth.

The ice of the along-flow profile shows much less source induced noise (Figure 4c) than the across-flow profile. The far eastern end (upstream) of the profile also shows the diamond shaped pattern caused by reflecting direct wave fronts. The ice–bed contact has a positive polarity throughout the profile except at the flank (between 4,000 and 3,500 m) at the onset of the trough. The ice–bed contact in the trough itself is positive. The polarities of the top (ice–bedform contact) and bottom (bedform–bed contact as far as this can be determined) of the bedform are both positive. The three reflections r475, r590, and r630 are most clear from 3,200 m to ~2,000 m and follow the ice–bed contact but r475 is a reflector with a larger amplitude and can be tracked throughout the entire profile and roughly follows the bed at both the across- and along-flow profile.

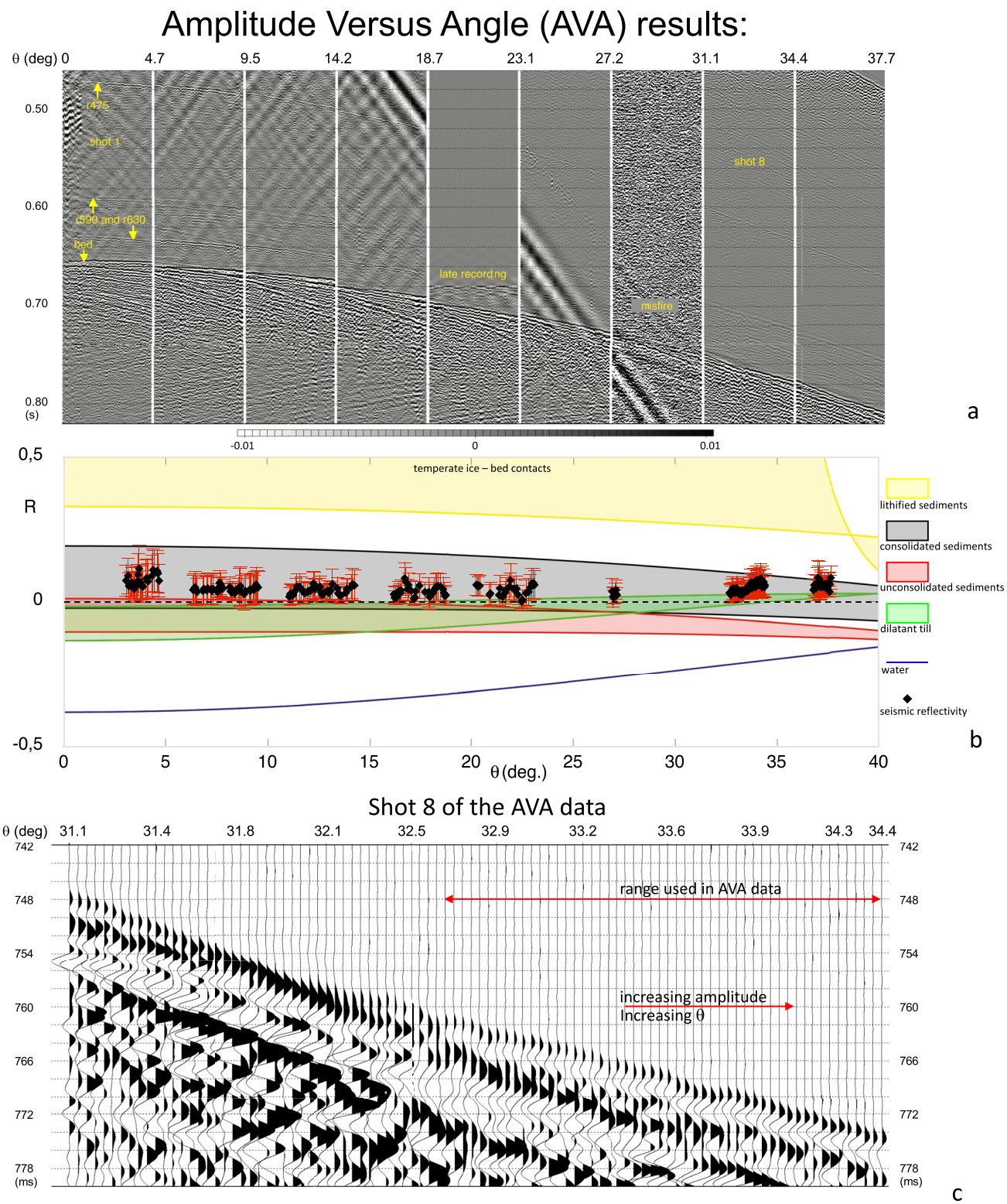

Figure 6. The Amplitude versus Angle (AVA) data set: (a) Nine shots forming the AVA data set to calculate $R(\theta)$ over the range $0° \leq \theta \leq 40°$. Shot 7 is a misfire which is why it appears noisy and is not used in the analysis. (b) Range of $R(\theta)$ for various material boundaries (colored areas). The calculated $R(\theta)$ from the eight shots (shot 7 is a misfire) mostly fits the temperate ice–consolidated sediments interval but shows a clear increasing trend after $\theta > 30°$. (c) A zoom of the ice–bed reflection of shot 8. The double-headed arrow marks the traces we used in the AVA analysis where the waves are reflecting at the bedform. There is a clear increasing trend of the amplitude toward the center of the lens-shaped bedform.

Table 2
Velocity Ranges of V_P, V_S, Densities of Temperate Ice and Subglacial Media Used to Determine R(θ) and R-Values at Normal Incidence of Temperate Ice and Subglacial Media

Lithology	V_P range (m/s)	V_S range (m/s)	ρ range (kg/m^3)	R range
Lithified sediments	3,000–6,200	1,200–3,400	2,200–2,800	0.31–0.69
Consolidated sediments	2,000–2,600	1,000–1,400	1,600–1,900	−0.04–0.21
Unconsolidated sediments	1,700–1,900	900–1,200	1,600–1,800	−0.12–0.04
Dilatant till	1,600–1,800	100–500	1,600–1,800	−0.15–0.01
Water	1,450–1,498	0	1,000–1,020	−0.41–−0.35
Temperate ice	3,470–3,740	1,670–1,880	917–921	

We determined R at normal incidence at four locations on the ice-bed interface (Figure 4b). At the bed (4,400 m) east of the trough flank entering the trough system $R \approx 0.18 \pm 0.20$, at the flank (3,750 m) $R \approx -0.10 \pm 0.20$, at the lens-shaped bedform at 2,200 m, $R \approx 0.10 \pm 0.12$ and downstream of the lens-shaped bedform at 500 m $R \approx 0.15 \pm 0.20$. The profile-derived Φ decreases by ∼60 kPa in downstream direction, with its maximum at 5,000 m and its minimum 400 m. The lowest values of Φ are between 3,200 and 400 m.

By quantifying $R(\theta)$ over $0° \leq \theta \leq 40°$, we narrow down identification of the subglacial material at the ice–bed interface considerably (Figure 6). We performed the AVA-analysis at the cross-point of the seismic profiles in across-flow direction (Figure 1). The eight shots composing this AVA data set (Figure 6a, FK and BP filtered for display-purpose here) represent the ice–bed reflection against an increasing offset which is converted into θ-space. $R(\theta)$ (Figure 6b) appears in eight groups, each group representing one shot (shot 7 was a misfire and could not be used). The ice–bed reflections of shots 1 to 6 interfere with source induced noise (diamond shaped patterns and the direct S-wave) whereas shots 8 and 9 are not affected by this noise. This source induced noise interference caused $R(\theta)$ in shots 1 to 6 being more variable and thus have a higher uncertainty.

The ice–bed contact area of each shot slightly shifts southward with increasing θ (Figure 6a). The ice–bed contact of shots 1 to 6 consist entirely of the lens shaped bedform whereas at shots 8 and 9, the south side of the trough is also visible. At these shots we only used the area with the ice–lens-shaped bedform contact (Figure 6c).

To calculate $R(\theta)$ we used the exact KZ-equations (Aki & Richards, 2002) with the ranges of physical quantities (shaded areas) determining $R(\theta)$ listed in Table 2 and assumed the basal ice is temperate (Harrington et al., 2015; Llorens et al., 2020). Almost all values fall in the shaded area (gray) of a temperate ice–consolidated sediment contact. $R(\theta)$ appears constant over the interval $3° \leq \theta \leq 27°$ and then slightly increases over the interval $32° \leq \theta \leq 38°$.

4. Discussion

The RES surveys detected a flat area with increased bed reflectivity with otherwise considerable topography (bedslopes from 12° to 17°). This flat area is part of a subglacial trough system and, based on Φ and the modeled subglacial water routing, a hydrological pathway (Figure 1a). From 2002 to 2012 we know supraglacial lakes drained annually partly through hydrofracture in this area (Fitzpatrick et al., 2014). Over 2010 Christoffersen et al. (2018) report on several cascading supraglacial lake drainage events in this area, starting with the "spring event", during May 25–28. These drainage events cause local loss of basal traction, ice flow speed-up, and routing of subglacial water through the subglacial trough system of the survey area. Because Φ is close to, but not exactly at, a local minimum in this flat area (Figures 1b, 3b and 4b) and because it is within 170 m of the ELA, subglacial water may have been ponding water here as an active subglacial lake (Bowling et al., 2019; Lindbäck et al., 2015).

The basal reflectivity of the flat area derived from the RES survey is sensitive to the applied signal attenuation rate through the ice. The range of attenuation rates determined in this study using the two methods (Section 2.2) naturally give variation in the basal reflectivity, but it does not change the pattern of stronger reflectivity over the flat area compared to the surrounding. The calculated basal reflectivity might also be influenced by the geometry of the bed were a steeply dipping bed may give lower reflectivity. However, other similar flat surfaces in the data set of Lindbäck et al. (2014) do not show significantly increased reflectivity compared to surrounding steeper bed

topography. We also see the same increased reflectivity at the profiles parallel to the trough. This suggests that the stronger reflectivity over the flat surface in our study area is not only due to the geometry of the bed. Based on the strong (>10 dB) relative bed reflectivity detected in the subglacial trough and the unusual flat characteristic, we propose that it could be a subglacial lake or at least a saturated or a wet subglacial environment.

In the post melt season of September 2013, a subsequent seismic survey revealed a lens-shaped bedform at the base of the subglacial trough system. Comparing the dimensions of the lens-shaped bedform of the unmigrated seismic profiles (Figures 3c and 4c) with the unmigrated radar profile, showed that the dimensions of the lens-shaped bedform and the flat area of increased radar reflectivity were similar in width and upstream (eastern) direction but 650 m shorter in downstream direction. This suggests the lens-shaped bedform caused, or at least that there is a connection with, the area of increased reflectivity. However, the values of R at normal incidence (single shots) of both seismic profiles (Figures 3b and 4b) indicate the lens-shaped bedform consists of consolidated sediments. The northern flank and the bed north of the trough do have negative values for R (Figure 3b), with the largest magnitude (most negative) value of R at the northern flank. As the magnitude of R at the bed north of the trough is smaller than at the flank our interpretation is that the bed north of the trough consists of less water saturated sediments that the flank itself. On the stoss side of the lens-shaped bedform stratification is parallel to the ice base suggesting the bedform was formed by several distinct sedimentation events. At the lee side the stratification is truncated, suggesting erosion. This truncated stratification at the lee side makes it unlikely the bedform is a drumlin (Woodard et al., 2020).

From the AVA analysis over lens-shaped bedform in across-flow direction, we calculated $R(\theta)$ over the interval $0° \leq \theta \leq 40°$ (Figure 6). Most $R(\theta)$ values fall within the temperate ice–consolidated sediment interface (gray area). But unlike the decreasing $R(\theta)$ with increasing θ trend we would expect at such an interface, we see an increasing $R(\theta)$ with increasing (θ). That this increasing trend of $R(\theta)$ is real and not an uncertainty becomes especially clear at larger θ ($32° \leq \theta \leq 38°$, shots 8 and 9) for three reasons: First, these shots are not affected by the source induced noise (Figure 6a) as shots 1 to 6 are. Second, we see this trend within a single shot, shot 8, and thus with a constant A_0 whereby $R(\theta)$ increases toward the center of the lens-shaped bedform (Figures 6b and 6c). Third, the $R(\theta)$-values of shot 9 are higher than of shot 8 thus the increasing trend is not restricted to a single shot. One could argue that $R(\theta)$ of shot 8 simply increases because material properties vary over this CDP-area but that is contradicted by the third reason, the $R(\theta)$-values of shot 9 are higher than those of shot 8 thus the increasing trend is not restricted to a single shot but to an ensemble of ray paths. Albeit being small we consider this trend to be real. It is as important for the interpretation of the AVA data as the $R(\theta)$-values themselves. This trend can be explained by an ice-water or an ice-dilatant till interface. Our interpretation is that the lens-shaped bedform we see in the seismic profiles does indeed consist of consolidated sediments but the increase in $R(\theta)$ with increasing θ is probably caused by a thin layer of dilatant till overlying the lens-shaped bedform. This layer can not be distinguished by the resolution of the seismic data ($d \leq 0.25\lambda$ with $\lambda \approx 10$ m is the wavelength of the center frequency of the seismic data), but does affect the determined $R(\theta)$ (Booth et al., 2012; Kulessa et al., 2017) and becomes apparent at larger $\theta \geq 32°$. As we use the exact KZ-equations instead of an approximation, $R(\theta)$ can be determined reliably over the interval $0° \leq \theta \leq 40°$ (Booth et al., 2016).

Our glaciological interpretation is that the lens-shaped bedform consists mostly of consolidated sediments but is overlain by a thin layer of saturated dilatant till, too thin to fully resolve with seismic data (2–3 m), that was deposited by transient subglacial meltwater. The 37 m thick, stratified lens-shaped bedform suggest local and repeated sediment deposition, of a glaciofluvial nature, over a longer period. The RES surveys suggest a subglacial lake or a wet subglacial environment such as dilatant till over the area of the lens-shaped bedform. The subglacial water from the supraglacial lake drainage events, reported by Fitzpatrick et al. (2014) and Christoffersen et al. (2018), likely followed the modeled subglacial drainage pathway thereby passing the area of the lens-shaped bedform and may have carried sediments. While establishing a subglacial drainage pathway, the water may have ponded temporarily at the bedform, depositing sediments, forming the lens-shaped bedform over time and over many occasions before this subglacial water was being transported downstream through the subglacial trough system. This process caused an increased reflectivity in the RES surveys where Φ has its lowest values (Figures 3b and 4b). That the dimensions of the bedform in downstream direction terminate 650 m upstream of the possible ponding area is not unusual for active lakes, they change in size over time. In September 2013 the sediments north of the trough and more so at the northern flank were still water-bearing. The area north of the flank, a topographic high, acts as a reservoir conform the observation of Chu et al. (2016) and is connected to the trough system. Interestingly the water bearing sediments of the across-flow profile (Figure 3) do not occur south of the trough

where Φ has its lowest values, but north of the trough where Φ is significantly higher. Φ indicates where subglacial conditions are favorable for water storage but it's the properties of the subglacial material that determine if water can be stored or not. The seismic survey performed in the post melt season of September 2013 does not give us evidence to distinguish if these possible ponding events would classify as an active subglacial or seasonal subglacial lake. Considering the location in the upper ablation area and following the classification of Bowling et al. (2019) we could expect the bedform was created by an active lake that filled and drained over decadal or shorter time scales, not a seasonal subglacial lake.

More evidence of ponding subglacial meltwater comes from the closed crevasse patterns. Judging by the diamond shaped patterns in the upper ice, mostly in the across-flow profile, most of these crevasses are orientated parallel to the ice flow (Appendix A). They mostly show up around the trough at the northern and southern flanks (Figure 3c) and at its eastern flank (Figure 4c), in other words, around the lens-shaped bedform. Christoffersen et al. (2018) explain these crevasses may occur after a tensile shock: supraglacial drainage water found its way to the bed through moulins or crevasses reducing basal traction and inducing a tensile stress perturbation. The lack of basal traction causes large longitudinal and transverse stresses causing extensional and transverse flow. Their modeling results show a significant increase in tensile stress in along- and across-flow direction after the supraglacial drainage events of 6–10 June 2010 in the survey area. These crevasses, parallel to the ice flow (Figure 3c), may well have formed by increased transverse ice flow which in its turn was a reaction to the increased longitudinal ice flow after the loss of basal traction causing crevasses perpendicular to the ice flow (Figure 4c). The location of the crevasses around the lens-shaped bedform indicates that the bedform likely is the area where the basal traction was reduced, in other words, where the supraglacial drainage water collected subglacially.

5. Conclusions

Our most important conclusion is that the lens-shaped bedform at the bed of the subglacial trough system mainly consists of consolidated sediments possibly overlain by a thin layer of dilatant till. The lens-shaped bedform clearly is a separate feature from the bed of the trough system so sediment deposition is a very local feature (1,750 m by 530 m) at this part of the glacier. As the extension of the radar data with increased reflectivity matches the extent of the lens-shaped feature well and the seismic data indicates the lens-shaped bedform is possibly overlain by a thin layer of dilatant till, temporarily ponding subglacial water may well have formed the lens-shaped bedform over longer time. As the radar data, indicating subglacial water, were collected in May 2010 and April 2011, water may have ponded here as part of the "spring event" that triggers cascading supraglacial lake drainage that was reported later that year by Christoffersen et al. (2018) and Fitzpatrick et al. (2014). We see water-bearing sediments at the elevated bed north of the trough system but not on the south side (Figure 3b). This last observation matches the interpretation of Kulessa et al. (2017) who interpreted the northern side of their survey area (which matches our southern side) as consolidated sediments.

From this survey it is clear that identification of subglacial material is tricky and could not have been done properly using radar or seismic profiling alone. Geophysical methods each have their own limitations. The radar profiles identified a possible subglacial lake based on the local flat bed with its increased reflectivity. A closer look using active seismic profiling revealed an elongated lens-shaped bedform, showing some stratification at the possible subglacial lake location. Based on R at normal incidence, determined from single shots, we would have identified the subglacial material of the lens-shaped feature as consolidated sediments but that raises the question as to why radar data showed increased reflectivity. This may have been caused by ponding subglacial meltwater or water containing sediments. The R-values at normal incidence determined from single seismic shots are blind to the presence of a thin layer of dilatant till overlying the lens-shaped bedform. The $R(\theta)$-values from the AVA data were essential to come to an interpretation that reconciled all geophysical observations.

Our results show that in particular small areas characterized as subglacial lakes by radar data, be it in Greenland, Antarctica or elsewhere, might be more ambiguous in composition, might change their properties over time and in fact represent rather more complex subglacial features than simple water bodies.

Appendix A: Three Representative Shot Records

In Figure A1a we present three representative BP filtered (30–550 Hz) shot records of Figure 3c (across-flow profile) respectively, north, at, and south of the trough system.

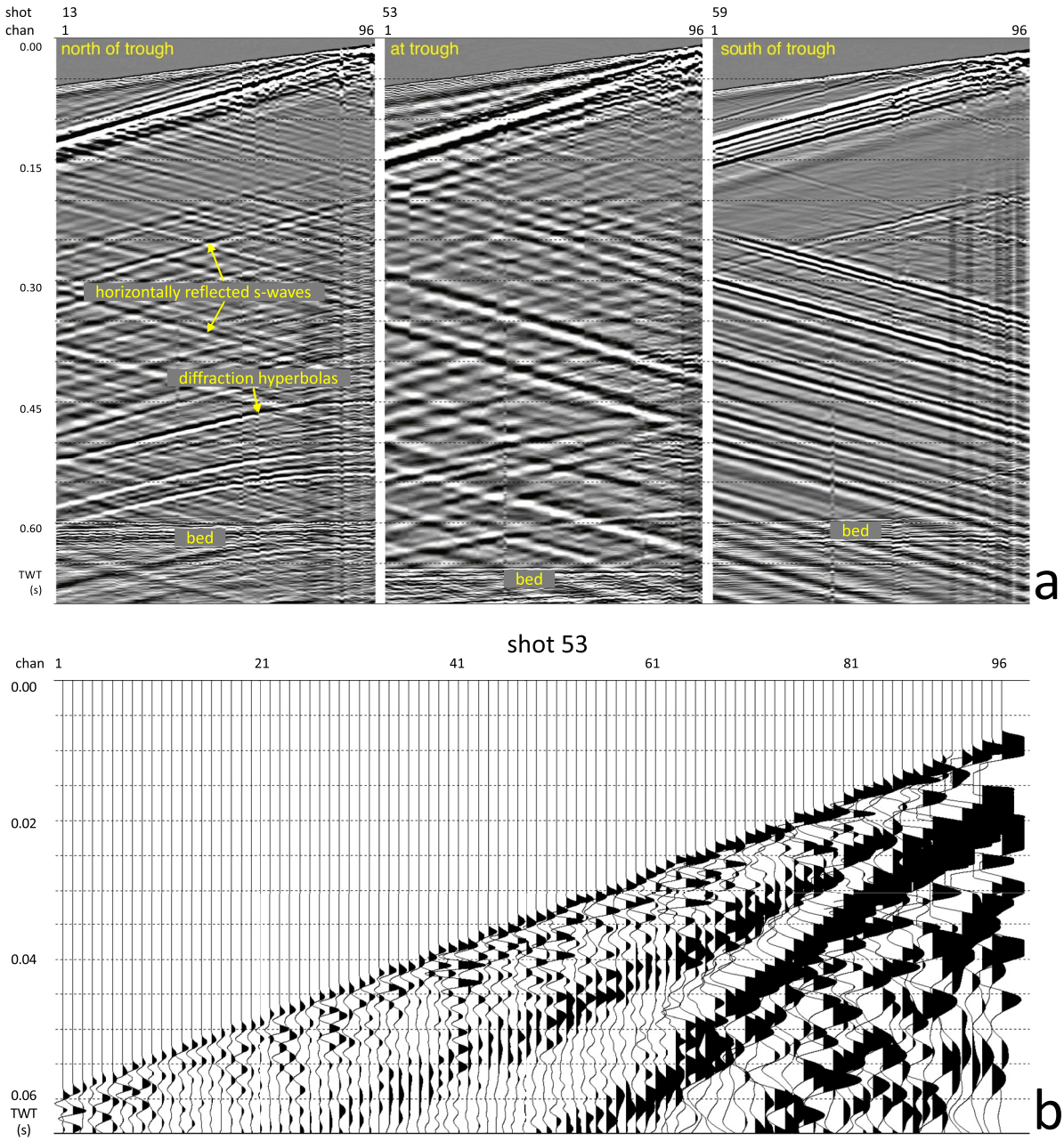

Figure A1. Three representative shots of the across-flow profile (Figure 3c) showing important characteristics we used to interpret the seismic data. (a) Shot 13 is representative for the area north of the trough, shot 53 for the area above the trough and shot 59 for the area just south of the trough. (b) Top 0.065 s of shot 53 showing the direct wave. The positive polarity of the P-wave, we define as positive, can clearly be made out.

Shot 13 is representative for 0–2,000 m of Figure 3c, the area north of the trough. The short record shows horizontally reflected S-waves forming diamond shaped patterns. Also visible in this area are diffraction hyperbola's typical for point sources. Our hypothesis is that these reflections are most likely caused by closed crevasses oriented parallel to the flow direction in the ice, behind and ahead of the shot location, nevertheless causing an interface which causes reflections. The direct S-wave reflects at several places along the streamer (traveling in southerly direction) which in turn reflect again and travel northward forming diamond shaped patterns through the shot record. The crevasses show up as short discontinuities (point sources) in the across-flow profile and form point source diffraction hyperbolas.

Shot 53 represents the trough system, 2,000–3,000 m of Figure 3c. Shot 53 is also the first shot of the AVA area. We see the same diamond shaped pattern and diffraction hyperbolas shot 13 shows. Our hypothesis is the same: the area above the trough most likely has closed crevasses oriented parallel to the ice-flow direction both behind and ahead of the shot location causing horizontally reflected direct waves in two directions.

Shot 59 represents the area south but close to the trough system, 3,000–3,600 m of Figure 3c. The shot record shows horizontally reflected S-waves but mainly from one direction: the reflections from behind the source (traveling in southerly direction). There are no diffraction hyperbolas visible. Our hypothesis is that the closed crevasses are behind (north of) this area and we hypothesize that they are probably located on the southern flank of the trough system.

Figure A1b shows the direct wave of shot 53. We define the polarity of the first arrival of the direct wave as positive. As we use dynamite cartridges in 2 m deep boreholes as a source we assume that the ice is compressed first by the spherically spreading P-wave and we define compression as positive. Based on this definition we distinguish a negative reflection (thus represented by extension) as reversed (negative) polarity. We also used the far field part of the direct wave (channel 40 to 1) to characterize the shape of the source wavelet.

Data Availability Statement

The seismic data set is available from the PANGAEA repository: Hofstede (2022): Seismic reflection data show a local sedimentation bedform at the subglacial trough system of Isunnguata Sermia, West Greenland, September 2013 [Dataset], https://doi.org/10.1594/PANGAEA.949168. The RES data from 2010 are included in Lindbäck et al. (2014). The RES data from 2011 are available at https://urn.kb.se/resolve?urn=urn:nbn:se:uu:diva-507866.

Acknowledgments

Some of the authors acknowledge the ice2sea project, funded by the European Commission's 7th Framework Programme through Grant 226375, manuscript No. ice2sea037. This research is part of ice2sea work package 2.2 and dedicated to the basal lubrication by surface melt. We thank captain Tore Sievertsen and Basse Vaengtoft for assistance in arranging local logistics. A special thanks to Sverrir Hilmarsson for his unwavering support in the field. The radar data was acquired under the SKB/Posiva funded Greenland Analog Project (GAP-SPB), and an RCUK (NERC) Grant NE/G005796/1. Field-logistics were kindly supported by the Royal Geographic Society and a Gilchrist Fieldwork Award. We acknowledge the invaluable contributions of the GAP (SPA) project field-team for safely collecting the RES data, particularly Katrin Lindbäck, Heïdi Sevestre and Christian Helanow. One of the authors, Alun Hubbard, does not agree with all statements made in the paper. Alun Hubbard gratefully acknowledges an Arctic Five Professorship, funding from the Research Council of Norway through its Centres of Excellence (iC3—Grant 332635), The University of Oulu—Arctic Interactions and the Academy of Finland PROFI4 Scheme (Grant 318930). Coen Hofstede would like to thank Aspen Technology, Inc. for providing software licenses and support. We thank the three reviewers, Adam Booth, Huw Horgan and the anonymous reviewer for their constructive comments that helped improve this manuscript. Open Access funding enabled and organized by Projekt DEAL.

References

Aki, K., & Richards, P. G. (2002). *Quantitative seismology* (2nd ed.). University Science Books Sausalito California.

Aschwanden, A., Fahnestock, M. A., & Truffer, M. (2016). Complex Greenland outlet glacier flow captured. *Nature Communications*, *7*(1), 10524. https://doi.org/10.1038/ncomms10524

Bartholomew, I., Nienow, P., Douglas, M., Hubbard, A., King, M., & Sole, A. (2010). Seasonal evolution of subglacial drainage and acceleration in a Greenland outlet glacier. *Nature Geoscience*, *3*(6), 408–411. https://doi.org/10.1038/ngeo863

Booth, A. D., Clark, R. A., Kulessa, B., Murray, T., Carter, J., Doyle, S., & Hubbard, A. (2012). Thin-layer effects in glaciological seismic amplitude-versus-angle (AVA) analysis: Implications for characterizing a subglacial till unit, Russell Glacier, West Greenland. *The Cryosphere*, *6*(4), 909–922. https://doi.org/10.5194/tc-6-909-2012

Booth, A. D., Emir, E., & Diez, A. (2016). Approximations to seismic AVA responses: Validity and potential in glaciological applications. *Geophysics*, *81*(1), 1–11. https://doi.org/10.1190/GEO2015-0187.1

Bougamont, M., Christoffersen, P., Hubbard, A., Fitzpatrick, A., Doyle, S. H., & Carter, S. P. (2014). Sensitive response of the Greenland Ice Sheet to surface melt drainage over a soft bed. *Nature Communications*, *5*(5052), 5052. https://doi.org/10.1038/ncomms6052

Bowling, J. S., Livingstone, S. J., Sole, A. J., & Chu, W. (2019). Distribution and dynamics of Greenland subglacial lakes. *Nature Communications*, *10*(1), 2810. https://doi.org/10.1038/s41467-019-10821-w

Carter, S. P., Blankenship, D. D., Peters, M. E., Young, D. A., Holt, J. W., & Morse, D. L. (2007). Radar-based subglacial lake classification in Antarctica. *Geochemistry, Geophysics, Geosystems*, *8*(3), Q03016. https://doi.org/10.1029/2006GC001408

Chandler, D. M., & Hubbard, A. (2023). Widespread partial-depth hydrofractures in ice sheets driven by supraglacial streams. *Nature Geoscience*, *16*(7), 605–611. https://doi.org/10.1038/s41561-023-01208-0

Christoffersen, P., Bougamont, M., Hubbard, A., Doyle, S. H., Grigsby, S., & Pettersson, R. (2018). Cascading lake drainage on the Greenland ice sheet triggered by tensile shock and fracture. *Nature Communications*, *9*(1), 1064. https://doi.org/10.1038/s41467-018-03420-8

Chu, W., Schroeder, D. M., Seroussi, H., Creyts, T. T., Palmer, S. J., & Bell, R. E. (2016). Extensive winter subglacial water storage beneath the Greenland ice sheet. *Geophysical Research Letters*, *43*(24), 12484–12492. https://doi.org/10.1002/2016GL071538

Davison, B. J., Sole, A. J., Livingstone, S. J., Cowton, T. R., & Nienow, P. W. (2019). The influence of hydrology on the dynamics of land-terminating sectors of the Greenland ice sheet. *Frontiers in Earth Science*, *7*, 10. https://doi.org/10.3389/feart.2019.00010

Doyle, S. H., Hubbard, A., Fitzpatrick, A. A. W., van As, D., Mikkelsen, A. B., Pettersson, R., & Hubbard, B. (2014). Persistent flow acceleration within the interior of the Greenland ice sheet. *Geophysical Research Letters*, *41*(3), 899–905. https://doi.org/10.1002/2013GL058933

Doyle, S. H., Hubbard, A. L., Dow, C. F., Jones, G. A., Fitzpatrick, A., Gusmeroli, A., et al. (2013). Ice tectonic deformation during the rapid in situ drainage of a supraglacial lake on the Greenland ice sheet. *The Cryosphere*, *7*(1), 129–140. https://doi.org/10.5194/tc-7-129-2013

Fitzpatrick, A. A. W., Hubbard, A. L., Box, J. E., Quincey, D. J., van As, D., Mikkelsen, A. P. B., et al. (2014). A decade (2002–2012) of supraglacial lake volume estimates across Russell Glacier, West Greenland. *The Cryosphere*, *8*(1), 107–121. https://doi.org/10.5194/tc-8-107-2014

Harper, J. T., Humphrey, N. F., Meierbachtol, T. W., Graly, J. A., & Fischer, U. H. (2017). Borehole measurements indicate hard bed conditions, Kangerlussuaq sector, western Greenland Ice Sheet. *Journal of Geophysical Research: Earth Surface*, *122*(9), 1605–1618. https://doi.org/10.1002/2017JF004201

Harrington, J. A., Humphrey, N. F., & Harper, J. T. (2015). Temperature distribution and thermal anomalies along a flowline of the Greenland ice sheet. *Annals of Glaciology*, *56*(70), 98–104. https://doi.org/10.3189/2015AoG70A945

Hoffman, M. J., Andrews, L. C., Price, S. F., Catania, G. A., Neumann, T. A., Lüthi, M. P., et al. (2016). Greenland subglacial drainage evolution regulated by weakly connected regions of the bed. *Nature Communications*, *7*(1), 13903. https://doi.org/10.1038/ncomms13903

Hofstede, C. M. (2022). Seismic reflection data show a local sedimentation bedform at the subglacial trough system of Isunnguata Sermia, West Greenland, September 2013. PANGAEA. https://doi.org/10.1594/PANGAEA.949168

Holland, C., & Anandakrishnan, S. (2009). Subglacial seismic reflection strategies when source amplitude and medium attenuation are poorly known. *Journal of Glaciology*, *55*(193), 931–937. https://doi.org/10.3189/002214309790152528

Horgan, H. J., van Haastrecht, L., Alley, R. B., Anandakrishnan, S., Beem, L. H., Christianson, K., et al. (2021). Grounding zone subglacial properties from calibrated active-source seismic methods. *The Cryosphere*, *15*(4), 1863–1880. https://doi.org/10.5194/tc-15-1863-2021

Hubbard, B., & Nienow, P. (1997). Alpine subglacial hydrology. *Quaternary Science Reviews*, *16*(9), 939–955. https://doi.org/10.1016/S0277-3791(97)00031-0

Humbert, A., Steinhage, D., Helm, V., Beyer, S., & Kleiner, T. (2018). Missing evidence of widespread subglacial lakes at recovery glacier, Antarctica. *Journal of Geophysical Research: Earth Surface*, *123*(11), 2802–2826. https://doi.org/10.1029/2017JF004591

Jacobel, R. W., Welch, B. C., Osterhouse, D., Pettersson, R., & MacGregor, J. A. (2009). Spatial variation of radar-derived basal conditions on Kamb Ice Stream, West Antarctica. *Annals of Glaciology*, *50*(51), 10–16. https://doi.org/10.3189/172756409789097504

Joughin, I., Das, S. B., King, M. A., Smith, B. E., Howat, I. M., & Moon, T. (2008). Seasonal speedup along the western flank of the Greenland ice sheet. *Science*, *320*(5877), 781–783. https://doi.org/10.1126/science.1153288

Koziol, C., Arnold, N., Pope, A., & Colgan, W. (2017). Quantifying supraglacial meltwater pathways in the Paakitsoq region, West Greenland. *Journal of Glaciology*, *63*(239), 464–476. https://doi.org/10.1017/jog.2017.5

Kulessa, B., Hubbard, A. L., Booth, A. D., Bougamont, M., Dow, C. F., Doyle, S. H., et al. (2017). Seismic evidence for complex sedimentary control of Greenland ice sheet flow. *Science Advances*, *3*(8), e1603071. https://doi.org/10.1126/sciadv.1603071

Lindbäck, K., Pettersson, R., Doyle, S. H., Helanow, C., Jansson, P., Kristensen, S. S., et al. (2014). High-resolution ice thickness and bed topography of a land-terminating section of the Greenland ice sheet. *Earth System Science Data*, *6*(2), 331–338. https://doi.org/10.5194/essd-6-331-2014

Lindbäck, K., Pettersson, R., Hubbard, A. L., Doyle, S. H., van As, D., Mikkelsen, A. B., & Fitzpatrick, A. A. (2015). Subglacial water drainage, storage, and piracy beneath the Greenland ice sheet. *Geophysical Research Letters*, *42*(18), 7606–7614. https://doi.org/10.1002/2015gl065393

Livingstone, S. J., Li, Y., Rutishauser, A., Sanderson, R. J., Winter, K., Mikucki, J. A., et al. (2022). Subglacial lakes and their changing role in a warming climate. *Nature Reviews Earth & Environment*, *3*(2), 106–124. https://doi.org/10.1038/s43017-021-00246-9

Livingstone, S. J., Sole, A. J., Storrar, R. D., Harrison, D., Ross, N., & Bowling, J. (2019). Brief communication: Subglacial lake drainage beneath Isunguata Sermia, West Greenland: Geomorphic and ice dynamic effects. *The Cryosphere*, *13*(10), 2789–2796. https://doi.org/10.5194/tc-13-2789-2019

Llorens, M.-G., Griera, A., Bons, P. D., Gomez-Rivas, E., Weikusat, I., Prior, D. J., et al. (2020). Seismic anisotropy of temperate ice in polar ice sheets. *Journal of Geophysical Research: Earth Surface*, *125*(11), e2020JF005714. https://doi.org/10.1029/2020JF005714

MacGregor, J. A., Winebrenner, D. P., Conway, H., Matsuoka, K., Mayewski, P. A., & Clow, G. D. (2007). Modeling englacial radar attenuation at Siple Dome, West Antarctica, using ice chemistry and temperature data. *Journal of Geophysical Research*, *112*(F3), F03008. https://doi.org/10.1029/2006JF000717

Morlighem, M., Williams, C. N., Rignot, E., An, L., Arndt, J. E., Bamber, J. L., et al. (2017). Bedmachine v3: Complete bed topography and ocean bathymetry mapping of Greenland from multibeam echo sounding combined with mass conservation. *Geophysical Research Letters*, *44*(21), 11051–11061. https://doi.org/10.1002/2017GL074954

Noël, B., van de Berg, W. J., Lhermitte, S., & van den Broeke, M. R. (2019). Rapid ablation zone expansion amplifies north Greenland mass loss. *Science Advances*, *5*(9), eaaw0123. https://doi.org/10.1126/sciadv.aaw0123

Palmer, S., McMillan, M., & Morlighem, M. (2015). Subglacial lake drainage detected beneath the Greenland ice sheet. *Nature Communications*, *6*(1), 8408. https://doi.org/10.1038/ncomms9408

Palmer, S. J., Dowdeswell, J. A., Christoffersen, P., Young, D. A., Blankenship, D. D., Greenbaum, J. S., et al. (2013). Greenland subglacial lakes detected by radar. *Geophysical Research Letters*, *40*(23), 6154–6159. https://doi.org/10.1002/2013GL058383

Ryser, C., Luethi, M., Andrews, L., Catania, G., Funk, M., Hawley, R., et al. (2014). Caterpillar-like ice motion in the ablation zone of the Greenland ice sheet. *Journal of Geophysical Research: Earth Surface*, *119*(10), 2258–2271. https://doi.org/10.1002/2013JF003067

Shreve, R. L. (1972). Movement of water in glaciers. *Journal of Glaciology*, *11*(62), 205–214. https://doi.org/10.3189/S002214300002219X

Sole, A., Nienow, P., Bartholomew, I., Mair, D., Cowton, T., Tedstone, A., & King, M. A. (2013). Winter motion mediates dynamic response of the Greenland ice sheet to warmer summers. *Geophysical Research Letters*, *40*(15), 3940–3944. https://doi.org/10.1002/grl.50764

Tedstone, A. J., Nienow, P. W., Gourmelen, N., Dehecq, A., Goldberg, D., & Hanna, E. (2015). Decadal slowdown of a land-terminating sector of the Greenland ice sheet despite warming. *Nature*, *526*(7575), 692–695. https://doi.org/10.1038/nature15722

van de Wal, R. S. W., Boot, W., Smeets, C. J. P. P., Snellen, H., van den Broeke, M. R., & Oerlemans, J. (2012). Twenty-one years of mass balance observations along the k-transect, West Greenland. *Earth System Science Data*, *4*(1), 31–35. https://doi.org/10.5194/essd-4-31-2012

van de Wal, R. S. W., Smeets, C. J. P. P., Boot, W., Stoffelen, M., van Kampen, R., Doyle, S. H., et al. (2015). Self-regulation of ice flow varies across the ablation area in south-west Greenland. *The Cryosphere*, *9*(2), 603–611. https://doi.org/10.5194/tc-9-603-2015

Woodard, J. B., Zoet, L. K., Benediktsson, Í. Ö., Iverson, N. R., & Finlayson, A. (2020). Insights into drumlin development from ground-penetrating radar at Múlajökull, Iceland, a surge-type glacier. *Journal of Glaciology*, *66*(259), 822–830. https://doi.org/10.1017/jog.2020.50